Ab initio atomistic simulation of the strength of defective aluminum and tests of empirical force models

V.B. Deyirmenjian,* V. Heine, M.C. Payne, and V. Milman†
Cavendish Laboratory, Theory of Condensed Matter, Madingley Road, Cambridge CB3 0HE, United Kingdom

R.M. Lynden-Bell‡
University Chemistry Laboratory, Lensfield Road, Cambridge CB2 1EW, United Kingdom

M.W. Finnis‡
Max-Planck-Institut für Metallforschung, Institut für Werkstoffwissenschaft, Seestrasse 92, D-7000 Stuttgart 1, Germany
(Received 7 March 1995; revised manuscript received 11 July 1995)

The effects of atomic-scale voids on the strength and mechanical behavior of aluminum at zero temperature are investigated using the total-energy pseudopotential method. A series of calculations are performed in which the defective system is extended by a small increment and then is relaxed to its ground state configuration. The total energy and stress are determined at each level of strain. The "tensile test" of the defective system is compared with the results of an experiment on a perfect system. These simulations employ a quantum mechanical scheme and show the processes of deformation around the defects including the initiation of dislocations and slip. They can also be used as a database on which to test models based on simpler atomistic potentials. We use them in that way to test a Sutton-Chen model tuned to our quantum mechanically simulated system, and a pairwise model by way of contrast to metallic bonding. The Sutton-Chen model shows significant void expansion at about 60% of the failure strain, an effect which is not seen in the *ab initio* calculations. The *ab initio* calculations suggest how empirical models such as the Sutton-Chen scheme can probably be improved to reflect better the nature of metallic bonding.

I. INTRODUCTION

An ideal crystal containing no defects can be extended under uniaxial tensile strain until the applied stress reaches a maximum, $\sigma_{\max}$ at strain $\epsilon_{\max}$. This theoretical value is a measure of the strength of the solid and marks the onset of instability. Any additional strain will result in the *failure* of the solid. In the case of *brittle* failure, the crystal breaks by *cleaving* into two sections. In contrast, *ductile* failure involves the material flowing apart by *shearing*.[1]

To understand how solids fail, it is necessary to establish a criterion for predicting the ductility or brittleness of materials. Kelly, Tyson, and Cottrell proposed that if the tensile stress σ at the tip of an atomically sharp crack exceeds $\sigma_{\max}$ before the shear stress τ (along a particular slip plane) exceeds $\tau_{\max}$, then the material is brittle.[2] The material is ductile if τ becomes larger than $\tau_{\max}$ first. Their theory was extended by Rice and Thomson who considered the conditions for the nucleation of dislocations from atomically sharp cracks.[3] If a dislocation is emitted before cleavage occurs, then the material is ductile. The descriptions of Kelly *et al.* and of Rice and Thomson are equivalent as demonstrated by Lin.[4] Both theories conclude, for example, that copper is ductile and that diamond is brittle, but neither approach can predict the behavior of materials which can undergo a brittle-ductile transition, such as iron.

Although the theories described above are important to our understanding of the mechanical behavior of materials, macroscopic behavior is in principle determined at the atomic rather than at the mesoscopic level. For example, cracks propagate via the breaking of interatomic bonds. Most experimental samples contain impurity atoms, which can act as sites of void nucleation.[5] Hence, atomistic simulations, or computer experiments as they are also known, can make substantial contributions to further elucidating the mechanical properties of solids such as their strength. However, these simulations are only as good as the model of the atomic interactions which they employ. The interatomic bonding determines all of the atomic positions and therefore defines the behavior of the simulated solid as it deforms, for example, under uniaxial tensile strain.

In the present work, the bonding in aluminum is represented by solving the nonrelativistic quantum mechanical equations (Schrödinger's equations) for an interacting many-electron system at every stage of the simulation. These quantum mechanical calculations are performed within the *total-energy pseudopotential method*, an "*ab initio*" scheme in which the only required input is the atomic number of the atoms.[6] The only approximations used in this method are the pseudopotential approximation to represent the valence electron-ion core interactions and the local-density approximation (LDA) for determining the exchange and correlation energy of the valence electrons. However, these approximations are known to be reasonable for well-bonded materials such as aluminum.[7]

The first goal of this investigation is to understand how a sample of aluminum containing atomic-scale voids fails as it is pulled apart at zero temperature (see Fig. 1). To be precise, our system contains lines of vacancies on nearest-neighbor sites forming thin pipes in the [110] direction. A series of *ab initio* calculations are performed in which the simulated defective solid is subjected to an increasing uniaxial tensile

 © 1995 The American Physical Society

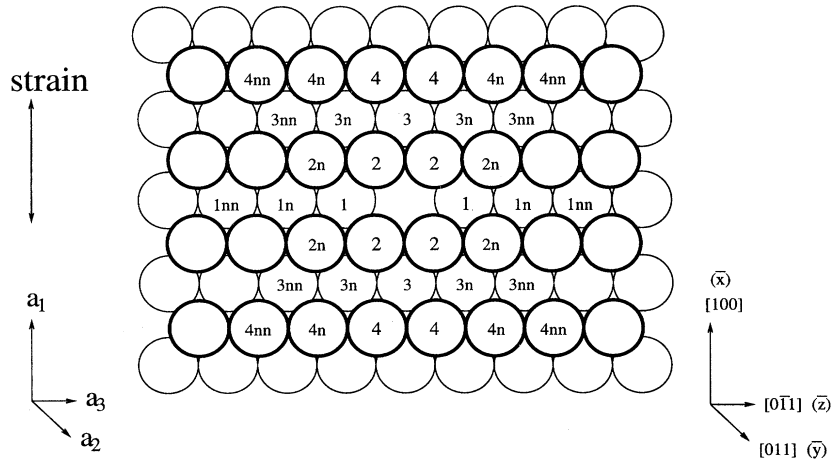

FIG. 1. Supercell used to model defects in aluminum. The periodic repetition of the supercell generates lines of vacancies which can be viewed as atomic-scale voids. The labels 1, $1n$, . . . ,4 identify atoms of interest. The thin and thick edged circles represent atoms in the planes $\bar{y}=0$ and $\bar{y}=\frac{1}{2}|\mathbf{a}_2|$ which are referred to as planes 1 and 2, respectively. A supercell with the same geometry as shown above, but without any removed atoms, is employed for the simulation of perfect aluminum. The coordinates $\bar{x}$, $\bar{y}$, and $\bar{z}$ measure the distance along the directions [100], [011], and [0$\bar{1}$1].

strain. At each discrete level of extension, the self-consistent total energy, stress, and equilibrium structure are determined, with the dimensions of the supercell held fixed. Similar calculations are performed for a perfect system containing no defects. The stress-strain curves of the two systems are compared in order to measure the effect of the defects on the strength of the simulated aluminum.

The simulations are analyzed in terms of "local" quantities, namely, the atomic displacements and the strains of tetrahedra which link nearest-neighbor atoms. Since the forces on the atoms in the perfect system are zero at each level of global strain, there are no atomic relaxations and the ideal solid extends uniformly. In the defective system, atoms 1, 2, 3, and 4 (see Fig. 1) initially relax towards the center of the voids, but as the global strain increases, these atoms eventually move away from the defects. Large local strains develop in the region close to the voids as a result of these outward relaxations. The other atoms in the system remain near sites of uniform extension.

The simulations are also described in terms of "global" quantities, namely, the total energy and the average stress on the periodically repeated supercell. For both the perfect and defective systems, the stress in the direction of the applied global strain begins at about zero, increases as a function of the global strain, and reaches a maximum $\sigma_{\max}$ at strain $\epsilon_{\max}$. For strains greater than $\epsilon_{\max}$, the perfect system continues to extend uniformly. The atoms in the defective system continue to move away from the defects. A global strain is eventually reached where the stress and energy decrease rapidly. The material shears along planes with normals at about 45° to the axis of tensile strain. These processes are similar to ductile phenomena which occur in real solids.

The representation of metallic bonding in these *ab initio* calculations plays a crucial role in defining the atomistic processes which lead to failure. One way of describing metallic cohesion is in terms of the distribution of the atoms. The atoms in a metal tend to spread themselves apart from one another in order to establish a uniform distribution for a given atomic density. The resistance to changes in uniformity of the atomic configuration can be viewed as the reason why the defective solid deforms by shearing rather than by cleaving into two pieces.

The second purpose of this work is to use the *ab initio* calculations as a database for comparison with analogous simulations based on simpler atomistic models. In particular, we employ a Morse pair potential and a Sutton-Chen glue scheme to describe the atomic interactions. Although pair-potential models of solids have been used for many years, it is known that pairwise interactions are inadequate for representing the bonding in metals.[8] The Sutton-Chen glue scheme is derived from the Finnis-Sinclair approach[9] to include a basic aspect of metallic bonding. The Finnis-Sinclair model, the embedded atom method of Daw and Baskes,[10] and the effective medium theory[11] were designed to overcome some of the problems inherent in the pair-potential approach. However, these so-called "glue" methods have not been extensively tested against more exact approaches.

As expected, the pairwise model generates completely different failure processes from those observed in the quantum mechanical results. The brittle behavior of the defective solid in the pair-potential simulation emphasizes the role of metallic bonding in defining the ductility observed in the *ab initio* approach. However, for the glue model, where better agreement with the *ab initio* method is expected, there are nevertheless differences in basic quantities, such as the atomic volumes, at global strains well below the strain at which fracture takes place. The increased rate of outward

TABLE I. *Ab initio* calculations of the equilibrium lattice constant a_0, bulk modulus B_0, and elastic constants c_{11}, c_{12}, c_{44}, and c' using the supercell defining the test, perfect (Per), and defective (Def) systems. The experimental (Expt) values are extrapolations to zero temperature.

	Test	Per	Def	Expt
a_0 (Å)	3.98 ± 0.01[a]	-	-	4.02[b]
B_0 (GPa)	81 ± 3[a]	-	-	79.4[c]
c_{11} (GPa)	125 ± 2	135 ± 2	130 ± 2	114.3[c]
c_{12} (GPa)	65 ± 2	70 ± 2	66 ± 2	61.9[c]
c_{44} (GPa)	35 ± 2	35 ± 2	-	31.6[c]
$c=\frac{1}{2}(c_{11}-c_{12})$ (GPa)	30 ± 3	33 ± 3	32 ± 3	26.2[c]
$B=\frac{1}{3}(c_{11}+2c_{12})$ (GPa)	85 ± 3	92 ± 3	87 ± 3	79.4[c]

[a]Determined from E_{tot} vs lattice parameter a curve.
[b]P.K. Lam and M.L. Cohen (Ref. 22).
[c]G.N. Kamm and G.A. Alers (Ref. 23).

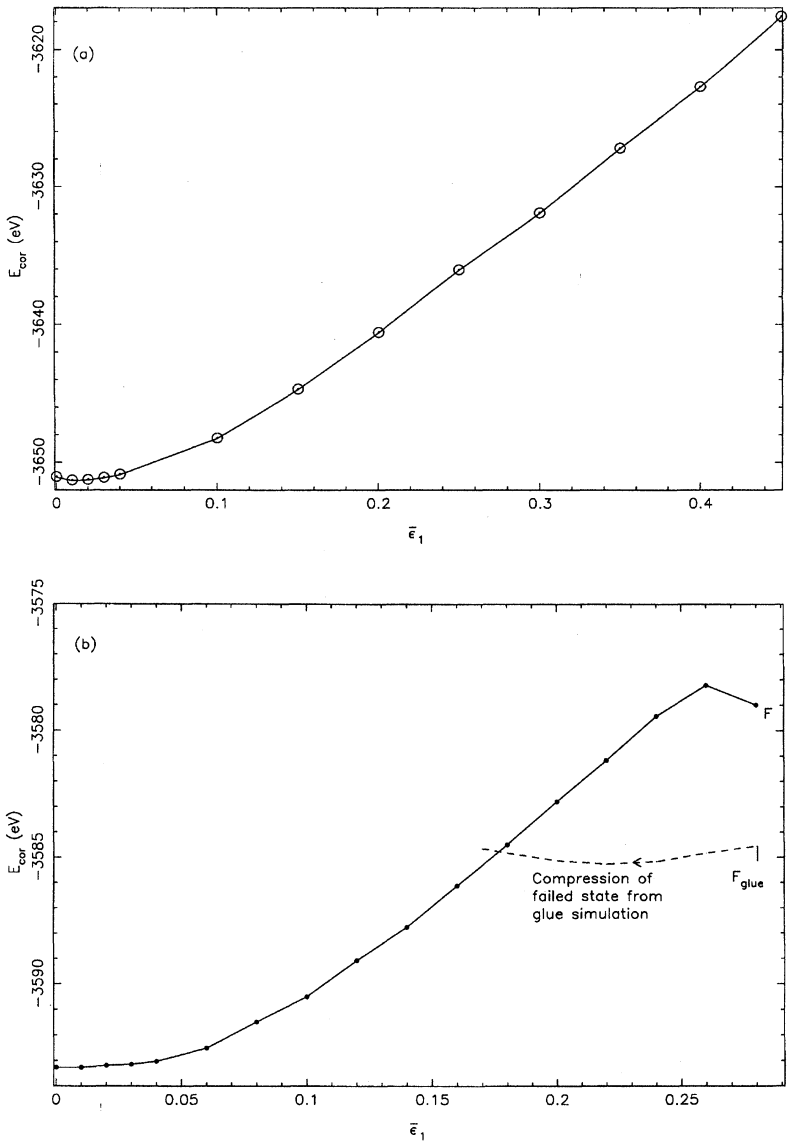

FIG. 2. Total energy E_{cor} as a function of strain $\bar{\epsilon}_1$ in the *ab initio* simulation for (a) the perfect system and (b) the defective system, where E_{cor} is the total energy per supercell extrapolated to zero smearing and corrected for the finite size of the plane wave basis set. The state at F in (b) is the relaxed configuration at $\bar{\epsilon}_1 = 0.28$. The relaxed configuration at F_{glue} is derived from the failed state which occurs in the glue simulation. The dashed line is the energy-strain path under uniaxial compression beginning at F_{glue}.

displacement of atoms away from the voids commences at much lower global strains in the glue simulation than in the *ab initio* simulation. It leads to a substantial and unphysical expansion of the void in the Sutton-Chen potential model.

The above research goals are presented as follows. In Sec. II, we outline our computer model. The *ab initio* computational approach is described in Sec. III. In Sec. IV, the results of the *ab initio* simulations are discussed. The quantum mechanical, pair-potential, and Sutton-Chen glue simulations are compared in Sec. V. The nature of metallic bonding and potential models is considered in Sec. VI. Conclusions about local deformations in the simulations are given in Sec. VII.

II. THE COMPUTER MODEL

The simulation of a solid under uniaxial tensile strain begins with the construction of a supercell containing atoms arranged in a realistic structure. Voids play an important role in the failure of ductile solids.[5] Unlike other types of defects, such as a crack with an atomically sharp tip, an elliptical cavity or void possessing dimensions on the order of angstroms can be studied using a periodically repeated supercell. In addition, the stress concentration around voids and cracks is qualitatively similar.

The supercell used to model a solid with atomic-scale voids (referred to as the defective system) contains 63 aluminum atoms, which are initially in fcc lattice positions (Fig. 1). The basis vectors which define the supercell are

$$\mathbf{a}_1 = 4(1+\bar{\epsilon}_1)a_0\hat{\mathbf{x}}, \tag{1}$$

$$\mathbf{a}_2 = \frac{\sqrt{2}}{2}a_0\hat{\mathbf{y}} ,$$

$$\mathbf{a}_3 = 4\sqrt{2}a_0\hat{\mathbf{z}} ,$$

where $\hat{\mathbf{x}}$, $\hat{\mathbf{y}}$, and $\hat{\mathbf{z}}$ are unit vectors in the directions [100], [011], and $[0\bar{1}1]$ referred to conventional cubic axes. The

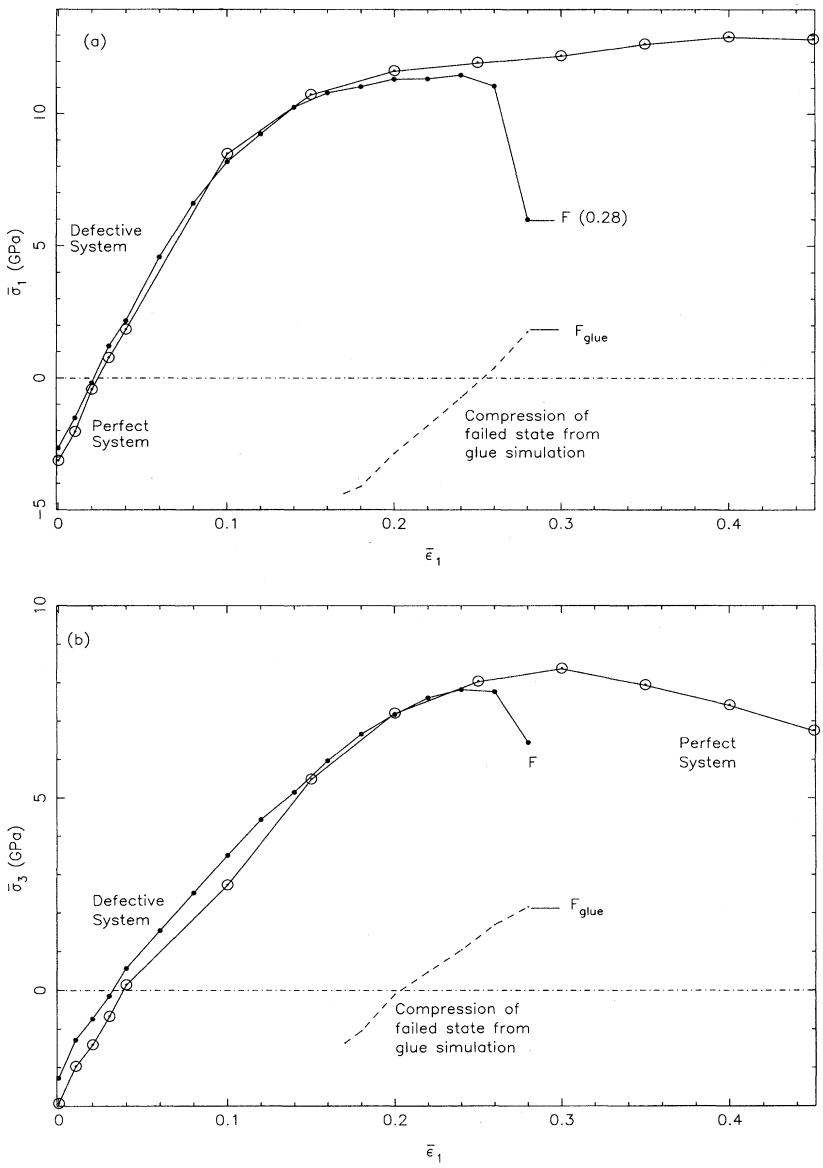

FIG. 3. (a) Stress $\bar{\sigma}_1$ on the surface of the supercell normal to the $\bar{x}$ direction as a function of strain $\bar{\epsilon}_1$ in the *ab initio* simulation. (b) Stress $\bar{\sigma}_3$ on the surface of the supercell normal to the $\bar{z}$ direction as a function of strain $\bar{\epsilon}_1$. The open and filled circles are the calculated points for the perfect and defective solids. The stresses are corrected using the Pulay expression, but are not extrapolated to zero smearing. The relaxed configuration at $\bar{\epsilon}_1 = 0.28$ is labeled F. The relaxed state at F_{glue} is derived from the failed state which occurs in the glue simulation. The dashed line is the stress-strain path under uniaxial compression beginning at F_{glue}.

equilibrium lattice parameter $a_0 = 3.98$ Å is determined using the test system described below. The strain $\bar{\epsilon}_1$ expands the supercell in the [100] direction. Since the supercell has only the thickness of one nearest-neighbor distance in the $\mathbf{a}_2$ direction, the periodic repetition of the supercell generates thin pipes on nearest-neighbor sites. These lines of vacancies can be viewed as extended atomic-scale voids. Slip in fcc solids takes place along {111} planes and in ⟨110⟩ directions.[1] The voids are oriented so that they run along the [011] direction, which is contained in the $(11\bar{1})$ and $(\bar{1}1\bar{1})$ slip planes. In order to compare directly the energies and stresses of the defective system with the energies and stresses of a perfect system, calculations are also performed using the above described supercell, but without removing any atoms.

The process of pulling a solid apart at zero temperature is simulated by increasing the uniaxial tensile strain $\bar{\epsilon}_1$ in small increments. The stress $\bar{\sigma}_\alpha$ and strain $\bar{\epsilon}_\alpha$ ($\alpha = 1, \ldots, 6$), are measured with respect to the coordinate system defined by the supercell basis vectors [Eq. (1)]. For a given value of the strain $\bar{\epsilon}_1$, the supercell dimensions are held fixed and the net forces on the atoms are used to relax the configuration to its ground state. The net forces on the atoms in the perfect system are zero and so there are no atomic displacements in the ideal crystal. The final total energy, stress, and atomic positions are recorded before expanding the supercell. The final atomic positions are used as the initial configuration for the next increment of strain.

III. *AB INITIO* COMPUTATIONAL METHOD

The calculations presented in this paper were performed using the Cambridge Serial Total-Energy Package (CASTEP), which is based on density-functional theory (DFT) in the local-density approximation.[6] In this method, the scattering properties of the ion cores (which will be referred to as atoms) are represented using nonlocal pseudopotentials in a

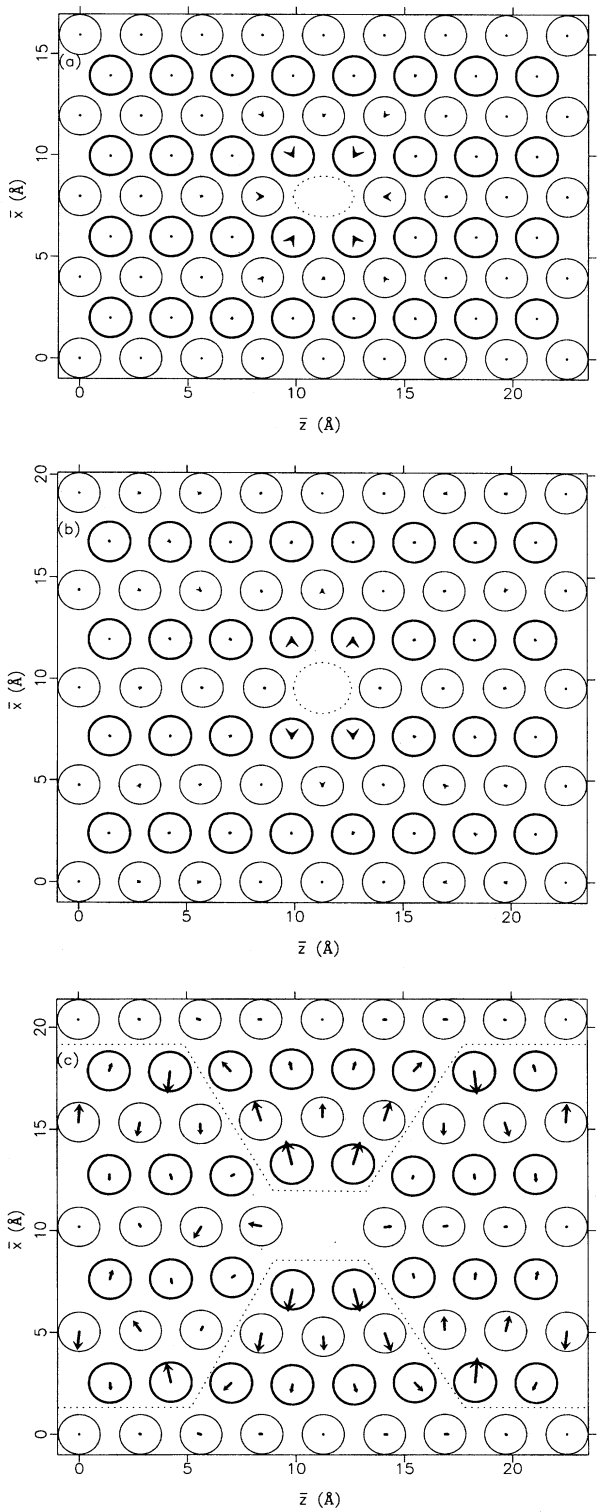

FIG. 4. Relaxed atomic positions in the *ab initio* simulation at $\bar{\epsilon}_1 =$ (a) 0.00, (b) 0.18, and (c) 0.26. The vectors indicate the positions to which the atoms relax when the system is expanded by $\Delta\bar{\epsilon}_1 =$ (a) 0.00, (b) 0.02, and (c) 0.02. The atoms in planes 1 and 2 are represented by thin and thick edged circles. The ellipse delineating the defect has major and minor axes defined by Eq. (8). In (c), shear deformations occur along the sides of the wedge structures which are bounded by the dotted lines and contain atoms 2, 3, $3n$, 4, and $4n$.

reciprocal space, Kleinman-Bylander representation.[12] Perdew and Zunger's[13] parametrization of the exchange-correlation energy is used. The valence electron orbitals are expanded in plane waves. The occupation of states is determined by the Gaussian-smearing method of Fu and Ho[14] as modified by Needs *et al.*[15] The conjugate-gradient method is employed to relax the electrons to their minimum energy configuration with the atoms held fixed.[16] The force on an atom due to the electrons in their ground state is determined by taking the derivative of the total energy of the system with respect to the position of the atom and using the Hellmann-Feynman theorem.[17] The Ewald summation method[18] is used to calculate the Coulomb contribution to the force on an atom due to the other atoms. Each atom is displaced by a small amount in the direction of the applied net force. The electronic system is relaxed to a new ground state, again with the atoms kept stationary. The cycle of atomic and electronic relaxations is continued until the net force on each atom is below a specific value, taken as 0.05 eV/Å.

The total energy per supercell $E_{\rm tot}$ is the central quantity determined in these calculations since most of the physical properties of solids can be related to changes in the total energy. However, the derivatives of $E_{\rm tot}$ also provide important information, as illustrated above in connection with the Hellmann-Feynman theorem. Another example is the average stress on the unit cell which can be calculated from

$$\sigma_{\alpha\beta}=\frac{1}{\Omega}\frac{\partial E_{\rm tot}}{\partial \epsilon_{\alpha\beta}} \ , \tag{2}$$

where Ω is the volume of the supercell and $\epsilon_{\alpha\beta}$ ($\alpha,\beta=1,2,3$) is the strain tensor, or from explicit formulas for the stress tensor based on DFT-LDA as given in Ref. 19.

The CASTEP program and the nonlocal aluminum pseudopotential were tested by determining the equilibrium lattice constant a_0, bulk modulus B_0, and elastic constants c_{11}, c_{12}, and c_{44}. The supercell for these calculations contained two atoms in a body-centered tetragonal cell which is referred to as the test system. The sampling of the Brillouin zone was accomplished by an $8\times8\times8$ Monkhorst-Pack scheme.[20] The energy cutoff for the plane wave basis set and the Gaussian-smearing width were 150 and 0.2 eV, respectively. The self-consistent calculations were performed until $E_{\rm tot}$ changed by less than 1 meV per iteration. The energies were corrected for the finite size of the plane wave basis set.[21] The stress tensor was computed using the expressions given in Ref. 19 and was corrected for the finite size of the plane wave basis set (i.e., the Pulay stress[21]).

The equilibrium lattice constant and bulk modulus were determined by calculating the total-energy per supercell as a function of the lattice parameter a. The data points were fitted by a quadratic polynomial using the least-squares method. The minimum of the fitted total-energy curve gave the theoretical equilibrium lattice constant a_0 and the second derivative at the minimum specified the equilibrium bulk modulus B_0.

The elastic constants c_{11}, c_{12}, and c_{44} were determined by applying small strains of order 0.004 to the test system. The results of these computations are presented in Table I and are in reasonable agreement with experiment. The result-

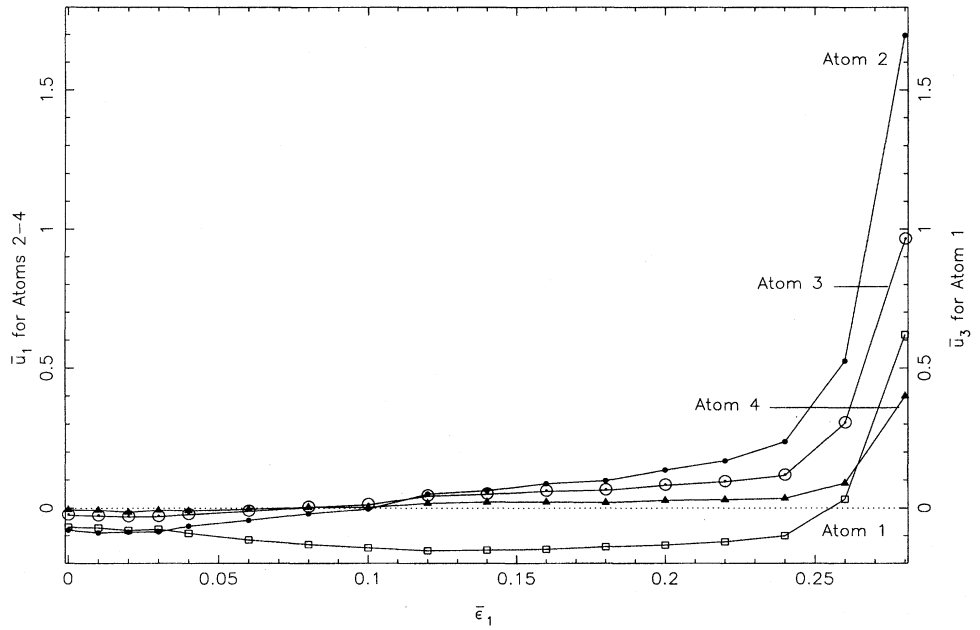

FIG. 5. Displacement $\bar{u}_3 = \bar{z}_{\text{rel}} - \bar{z}_{\text{unrel}}$ of atom 1 and $\bar{u}_1 = \bar{x}_{\text{rel}} - \bar{x}_{\text{unrel}}$ of atoms 2, 3, and 4 as a function of strain $\bar{\epsilon}_1$ in the *ab initio* simulation. The variables $\bar{z}_{\text{rel}}$ ($\bar{x}_{\text{rel}}$) and $\bar{z}_{\text{unrel}}$ ($\bar{x}_{\text{unrel}}$) refer to the $\bar{z}$ ($\bar{x}$) coordinate of atom 1 (atoms 2–4) in the relaxed and unrelaxed, uniformly strained defective system, respectively. Increases in $\bar{u}_1$ and $\bar{u}_3$ indicate displacements away from the center of the voids. The displacements of atoms 1, 2, 3, and 4 are represented by squares, filled circles, open circles, and triangles, respectively.

ing solid is an aluminumlike metal whose major metallic bonding aspects are the same as real aluminum.

The *ab initio* simulation of the defective system required the selection of parameters in the CASTEP code, including the energy cutoff $E_{\max}$ of the plane wave basis set, the Gaussian-smearing width Δ, and the Monkhorst-Pack scheme for sampling the Brillouin zone. The energy cutoff was reduced to 100 eV from the 150 eV cutoff employed for the test system in order to lower the computational time. The Brillouin zone sampling consisted of the k points $(0,\pm\frac{1}{8},0)$ and $(0,\pm\frac{3}{8},0)$, which can be expressed in terms of the reciprocal-space basis vectors

$$\mathbf{b}_1 = \frac{\pi}{2(1+\bar{\epsilon}_1)a_0}\hat{\mathbf{k}}_{\bar{x}} \ ,$$

$$\mathbf{b}_2 = \frac{2\sqrt{2}\pi}{a_0}\hat{\mathbf{k}}_{\bar{y}} \ , \tag{3}$$

$$\mathbf{b}_3 = \frac{\pi}{4a_0}\hat{\mathbf{k}}_{\bar{z}} \ .$$

These k points constitute a $1\times4\times1$ Monkhorst-Pack scheme. The sampling was limited to points along the direction of $\mathbf{b}_2$ since the vectors $\mathbf{b}_1$ and $\mathbf{b}_3$ were much smaller than $\mathbf{b}_2$. The Gaussian-smearing width was initially set to 0.2 eV. The elastic constant c_{11} of the perfect system determined by the $E_{\max}$, sampling grid, and Δ described above, was nearly twice as large as the experimentally determined value. The smearing width was therefore increased to 1.0 eV in order improve the effective sampling of the Brillouin zone.[15] However, the use of a large Gaussian-smearing width required the extrapolation of E_{tot} to the limit of zero broadening in order to determine the physically meaningful energy for the system at zero temperature.[24] This was accomplished by minimizing the "free energy" of the system

$$F = E_{\text{tot}} - S\Delta \ , \tag{4}$$

where S is an "entropy" correction term for the broadening of the electronic states.[24] The extrapolated energy, correct to second order in Δ, is

$$E_{\text{extrap}} = \tfrac{1}{2}(E_{\text{tot}} + F) \ . \tag{5}$$

The total energy per supercell, both extrapolated to zero smearing [Eq. (5)] and corrected for the finite size of the plane wave basis set in the manner of Ref. 21, is referred to as E_{cor}. It is shown in Fig. 2. The effect of the large smearing on the atomic forces was observed to be small. The forces determined using $\Delta = 0.5$ eV and the improved Brillouin zone sampling specified by a $1\times8\times1$ Monkhorst-Pack grid were not significantly different from the forces calculated using $\Delta = 1.0$ eV and a $1\times4\times1$ scheme. The stress $\bar{\sigma}_\alpha$, $\alpha = 1,\ldots,6$, determined by the expressions in Ref. 19, was not corrected for the smearing, but was corrected for the finite size of the plane wave basis set (Fig. 3). The stress

TABLE II. *Ab initio* and continuum theory calculations of maximum tensile strain $\epsilon_{\max}$ and stress $\sigma_{\max}$.

	$\epsilon_{\max}$	$\sigma_{\max}$ (GPa)
Defective solid[a]	0.18	11 ± 1
Perfect solid[a]	0.20	11 ± 1
Elastic solid[b]	0.23	20
Elastic solid[c]	0.29	16
Experimental[d]	0.029	2.25

[a]Determined from Figs. 3(a) and 3(b).
[b]Calculated using Eqs. (6) and (7) with $M = c_{11} = 135$ GPa (*ab initio* result with Poisson contraction absent), $\gamma = 0.074$ eV/Å^2 [from experiment (Ref. 25)], and $a_0 = 3.98$ Å (*ab initio* result).
[c]Calculated using Eqs. (6) and (7) with $M = (s_{11})^{-1} = 87$ GPa (*ab initio* result with Poisson contraction present). The values of γ and a_0 are as in footnote b.
[d]Gane (Ref. 26).

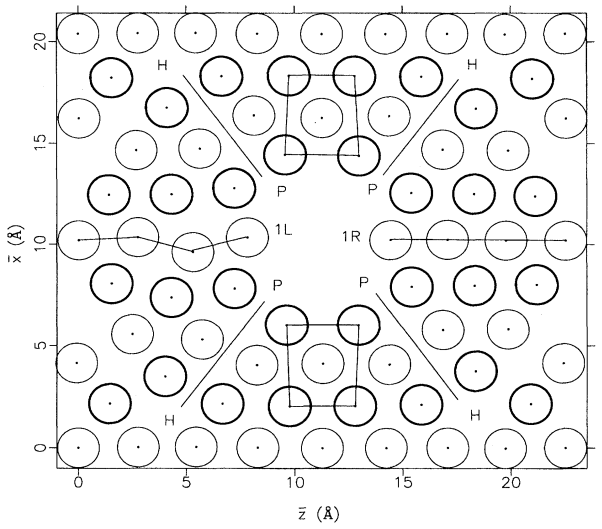

FIG. 6. Relaxed atomic positions at $\bar{\epsilon}_1=0.28$ in the *ab initio* simulation. The lines *HP* represent the planes along which shears take place.

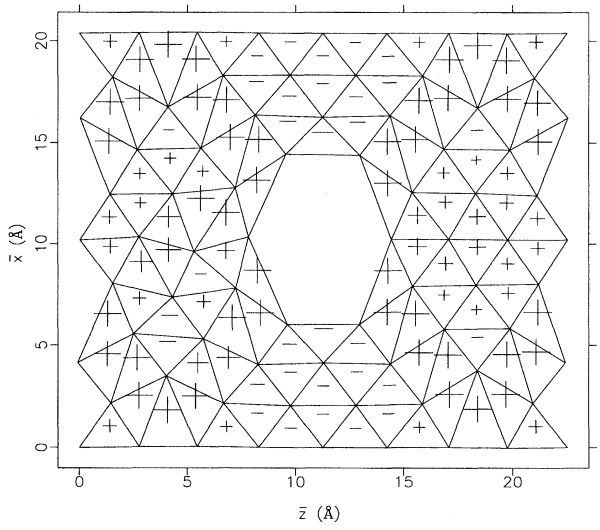

FIG. 7. Local orthorhombic shear strains $\bar{\epsilon}_{\text{locOS}}$ at $\bar{\epsilon}_1=0.28$ in the *ab initio* simulation. The "+" ("-") symbol represents a tensile (compressive) strain. The size of the symbols is scaled with respect to the largest orthorhombic shear strain which occurs in the entire simulation. The tetrahedra linking nearest-neighbor atoms are projected onto the (011) plane.

$\bar{\sigma}_1$ can be extrapolated to zero smearing and corrected for the finite size of the plane wave basis set by obtaining numerically the derivative of the E_{cor} vs $\bar{\epsilon}_1$ graph with respect to $\bar{\epsilon}_1$ and employing Eq. (2). It was observed that up to $\bar{\epsilon}_1=0.20$, the stresses from Ref. 19 and from the E_{cor} vs $\bar{\epsilon}_1$ graph were about the same. Beyond this level of strain, these stress calculations differed due to the limited accuracy of the numerical differentiation. Note that the zero of the stress-strain curves (Fig. 3) and the minimum of the $E_{\text{cor}}(\bar{\epsilon}_1)$ curve [Fig. 2(a)] for the perfect system are shifted slightly from $\bar{\epsilon}_1=0$. This is due to the use of the equilibrium lattice parameter a_0 found for the test system, with a different Brillouin zone sampling and Gaussian smearing. Since the amount of shift was small and different for each of the above relations, the figures were not adjusted to make the zero of stress and the minimum of energy at zero strain.

The stress-strain relations in Fig. 3 can be used to calculate the elastic constants c_{11} and c_{12} for both the perfect and defective systems as demonstrated for the test system. The slope of the stress-strain graphs at $\bar{\sigma}_\alpha=0$ ($\alpha=1,3$) gives the elastic constants c_{11} and c_{12}. The elastic constant c_{44} is determined by applying small shear strains $\bar{\epsilon}_6$ with $\bar{\epsilon}_\alpha=0$ ($\alpha=1,\ldots,5$), and measuring the resulting stresses $\bar{\sigma}_6$. These results are summarized in Table I, and agree with the elastic constants of the test calculation sufficiently for our purposes.

IV. DISCUSSION OF *AB INITIO* RESULTS

The tensile test experiments on the perfect and defective systems (Sec. II) are performed using the *ab initio* approach (Sec. III). To test convergence in atomic positions and strain increment $\Delta\bar{\epsilon}_1$, detailed tests were made with the glue model (see below) and less detailed (due to limitations of time) with the *ab initio* method. These showed that in the region $\bar{\epsilon}_1 \leq 0.16$ for the glue model and $\bar{\epsilon}_1 \leq 0.24$ for the *ab initio*, the system has a well-defined minimum for each $\bar{\epsilon}_1$, which is found more or less independent of $\Delta\bar{\epsilon}_1$ and the cutoff on the forces (when the relaxation is stopped and the supercell is expanded to the next value of $\bar{\epsilon}_1$). However, beyond these $\bar{\epsilon}_1$, when the rapid outward displacement of the central atoms occurs (see Fig. 5 and Fig. 15), the energy landscape is extremely flat. There are large areas of configurational space with very nearly the same energy. Here the results of the calculations depend sensitively on $\Delta\bar{\epsilon}_1$ and the cutoff on the forces. While the glue results (see below) are fully converged in all senses, the *ab initio* ones are not. To converge them would require several orders of magnitude more computer time, and it is even then not certain that the numerical accuracy would be sufficient. However, we believe the following conclusions remain qualitatively correct because they are also seen to varying degree in the fully converged glue results.

A measure of the strength of the perfect and defective solids is given by the maxima of the $\bar{\sigma}_1$ vs $\bar{\epsilon}_1$ relations (Fig. 3). It is remarkable how little difference there is between the maximum stress of the defective system $[\sigma_{\max}(D)]$ and the maximum stress of the perfect system $[\sigma_{\max}(P)]$, contrary to our expectation and contrary to the results with empirical atomic bonding models (see below). The strain $\epsilon_{\max}$ at which $\sigma_{\max}$ occurs is rather more difficult to determine due to noise in the calculated results and the fact that the maximum of the $\bar{\sigma}_1(\bar{\epsilon}_1)$ curve is so flat. Taking the results in Fig. 3 at face value, we would say $\sigma_{\max}(D)\approx$ 12 GPa and $\sigma_{\max}(P)\approx$ 13 GPa, but fitting a quartic curve to the energies $E_{\text{cor}}(\bar{\epsilon}_1)$ and differentiating this relation gives a lower value of about 11 GPa. This latter procedure indicates that $\epsilon_{\max}(D)\approx 0.18$ and $\epsilon_{\max}(P)\approx 0.20$.

A conventional theory based on a sinusoidal stress-strain relation for a perfect crystal under uniaxial tensile stress gives[1]

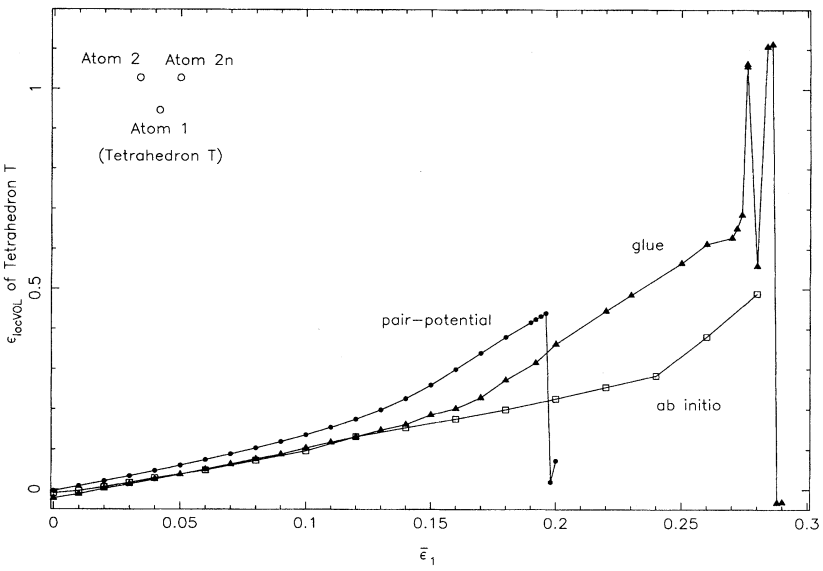

FIG. 8. Local volume strain $\bar{\epsilon}_{\text{locVOL}}$ of tetrahedron T in the defective system as a function of $\bar{\epsilon}_1$. The squares, filled circles, and triangles represent the calculated values in the *ab initio*, pair-potential, and glue simulations, respectively. Tetrahedron T links atoms 2, $2n$, 1, and the periodic image of atom 1 in the $\bar{y}$ direction.

$$\sigma_{\max}=\left(\frac{M\gamma}{a_0}\right)^{1/2}, \tag{6}$$

$$\epsilon_{\max}=\frac{\pi}{2}\frac{\sigma_{\max}}{M}, \tag{7}$$

where M is the appropriate elastic modulus, γ is the surface energy per unit area, and a_0 is the equilibrium lattice constant. The calculated maximum stress and associated strain sustained by the perfect system can be compared with Eqs. (6) and (7). When Poisson contraction, the reduction in the lateral dimensions of a test material, is not permitted and the strain is in the [100] direction, the modulus M equals c_{11}. The results shown in Table II are for $a_0=3.98$ Å, the equilibrium lattice constant used in the simulation of the perfect system, $c_{11}=135$ GPa, the elastic constant specified in Fig. 3(a), and $\gamma=\gamma_{100}\approx\gamma_{111}=0.074$ eV/Å^2 (Ref. 25), the surface energy of aluminum determined from experiment. For the simulated perfect solid, $\sigma_{\max}(P)$ and $\epsilon_{\max}(P)$ are about 45% and 10% smaller than the values determined in the above method. These differences occur since the stress-strain relation in Fig. 3(a) is not sinusoidal. Both the total-energy and continuum theory calculations predict strengths that are higher than in experiment due to a number of limitations. In real crystals, the motion of dislocations usually results in a reduction in strength.[1] However, there are no dislocations in the simulated perfect material or in the continuum model. The absence of Poisson contraction generally increases $\sigma_{\max}$. For example, when the dimensions perpendicular to the [100] strain direction are not constrained, $M=(s_{11})^{-1}=87$ GPa, where $s_{\alpha\beta}$ is the inverse of the elastic constant matrix $c_{\alpha\beta}$. The value of $\sigma_{\max}$ according to Eq. (6) is 25% higher when Poisson contraction is absent compared to when it is present (see Table II).

The significant decrease in the total energy [Fig. 2(b)] and stress (Fig. 3) as the defective solid is extended from $\bar{\epsilon}_1=0.26$ to $\bar{\epsilon}_1=0.28$ indicates that the system is on the point of fracture, as is even clearer in Fig. 4 and especially Fig. 5. We could not follow the system through its actual fracture due to the large computational resources that would have been required to determine the large atomic motions. However, a fractured state in the *ab initio* model is investigated by relaxing the failed state derived from a simulation

TABLE III. Morse pair-potential parameters determined from *ab initio* calculations of the equilibrium lattice constant a_0, elastic constant c_{11}, and void formation energy E_{void}. The elastic constants specified by the resulting pair potential are also shown. The cutoff R_{cut} of the Morse potential is 15 Å. The elastic constants are measured in units of GPa and $c'=\frac{1}{2}(c_{11}-c_{12})$.

ab initio constants	a_0	c_{11}	E_{void}		
	3.98 Å	130	1.0 eV		
Morse parameters	α	r_0	D		
	4.2171 Å^{-1}	2.8156 Å	0.16988 eV		
Elastic constants	c_{11}	c_{12}	c_{44}	c'	B_0
	130	75	75	28	93

TABLE IV. Sutton-Chen glue scheme parameters determined from *ab initio* calculations of the equilibrium lattice constant a_0, elastic constant c_{11}, and void formation energy E_{void}. The elastic constants specified by the resulting $(m,n)=(5,9)$ glue scheme are compared with those determined by the $(m,n)=(6,7)$ glue scheme. The cutoff of the potential is set to 20 Å. The elastic constants are measured in units of GPa and $c'=\frac{1}{2}(c_{11}-c_{12})$.

ab initio constants	a_0	c_{11}	E_{void}		
	3.98 Å	130	1.0 eV		
S-C parameters	m,n	c	ε		
	5,9	52.207	0.0091079 eV		
Elastic constants	c_{11}	c_{12}	c_{44}	c'	B_0
(5,9) scheme	103	75	43	14	85
(6,7) scheme	185	163	37	11	171

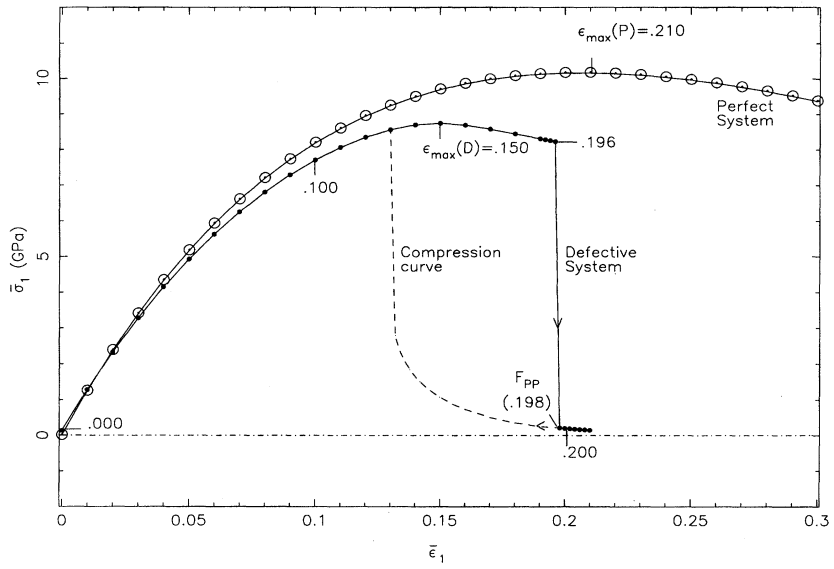

FIG. 9. Stress $\bar{\sigma}_1$ on the surface of the supercell normal to the $\bar{x}$ direction as a function of strain $\bar{\epsilon}_1$ in the pair-potential simulation. The open and closed circles represent the stresses on the perfect and defective systems calculated at increasing levels of tensile strain. The maximum tensile stresses on the perfect and defective systems occur at $\epsilon_{\max}(P)=0.210$ and $\epsilon_{\max}(D)=0.150$, respectively. The defective system fails at F_{PP} ($\bar{\epsilon}_1=0.198$). The stress-strain relation of the fractured state under compression (beginning at F_{PP}) is represented by the dashed line.

in which the interatomic bonding is based on the empirical glue scheme. The resulting ground state at the point F_{glue} ($\bar{\epsilon}_1=0.28$) in Fig. 2(b) has a much lower energy than the relaxed configuration at F. A series of calculations are performed using the configuration at F_{glue} as the initial state. The size of the system is decreased in strain increments of 0.02. At each level of compression, the supercell dimensions are fixed and the energy, stress, and ground state structure are determined. The stress and energy paths under compression and tension are distinct. In particular, the energy-strain curve under compression eventually intersects the original energy-strain relation under tensile strain just before $\epsilon_{\max}(D)\approx 0.18$ [Fig. 2(b)]. These lower energy configurations demonstrate that the states which are determined under tensile strain are metastable for $\bar{\epsilon}_1 > 0.18$.

Relaxed atomic configurations at several levels of tensile strain are visualized in Fig. 4. The individual motions of atoms 1, 2, 3, and 4 are shown in Fig. 5, following the atomic numbering given in Fig. 1. These figures are used to characterize the atomistic processes which result in the failure of the simulated solid. Note that the displacements in the [011] ($\bar{y}$) direction are zero by symmetry apart from some small numerical noise in the calculations.

At the microscopic level, the shape of a void is not uniquely defined. However, as a visual aid to interpreting the behavior of a simulated void, its shape can be described by an elliptic cylinder whose intersection with the (011) plane is an ellipse with major and minor axes

$$a_e=\tfrac{1}{2}|\bar{z}_{\text{center}}-\bar{z}_{\text{atom 1}}| \quad , \quad b_e=\tfrac{1}{2}|\bar{x}_{\text{center}}-\bar{x}_{\text{atom 2}}| \quad , \tag{8}$$

where $(\bar{x}_{\text{center}},\bar{y}=0,\bar{z}_{\text{center}})$ is the center of a void (referred to as V).

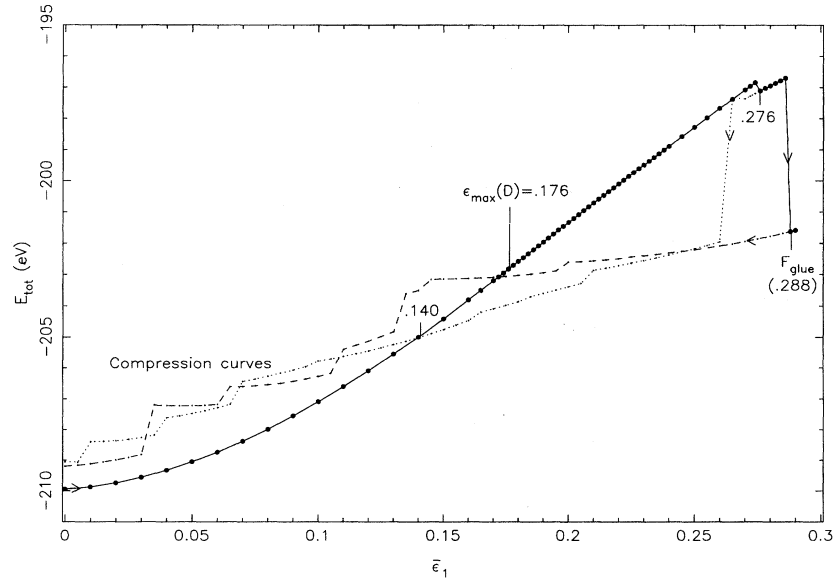

FIG. 10. Total energy E_{tot} of the defective system as a function of strain $\bar{\epsilon}_1$ in the glue simulation. The closed circles are the energies calculated at increasing levels of tensile strain. The maximum tensile stress occurs at $\epsilon_{\max}(D)=0.176$. The system fails at F_{glue} ($\bar{\epsilon}_1=0.288$). The energy-strain relation of the fractured state under compression (beginning at F_{glue}) is represented by the dashed line. The dotted line indicates the stress-strain path under compression beginning with the relaxed state at $\bar{\epsilon}_1=0.276$.

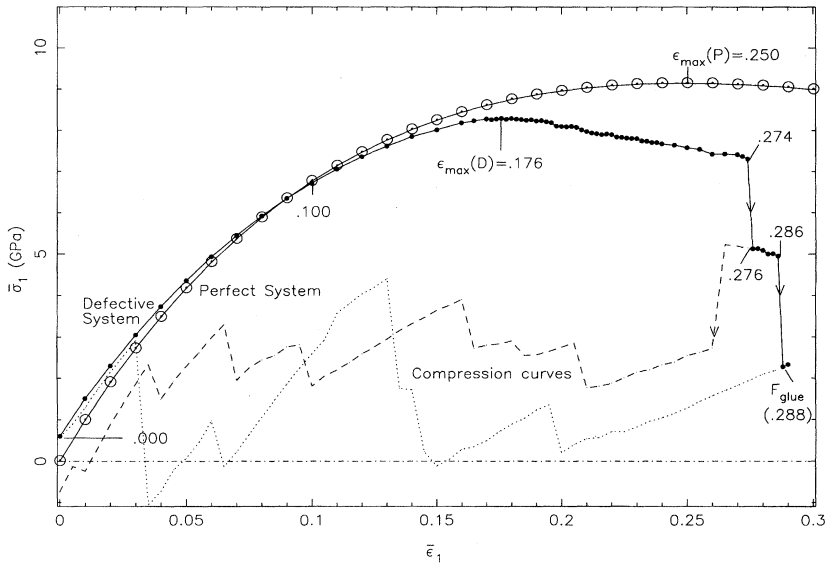

FIG. 11. Stress $\bar{\sigma}_1$ on the surface of the supercell normal to the $\bar{x}$ direction as a function of strain $\bar{\epsilon}_1$ in the glue simulation. The open and closed circles represent the stresses on the perfect and defective systems calculated at increasing levels of tensile strain. The maximum tensile stresses on the perfect and defective systems occur at $\epsilon_{max}(P)=0.250$ and $\epsilon_{max}(D)=0.176$, respectively. The defective system fails at F_{glue} ($\bar{\epsilon}_1=0.288$). The stress-strain relation of the fractured state under compression (beginning at F_{glue}) is represented by the dashed line. The dotted line indicates the stress-strain path under compression beginning with the relaxed state at $\bar{\epsilon}_1=0.276$.

Figure 4 reveals that the effects of the applied tensile strain of the supercell are initially concentrated on the atoms closest to the voids. For example, atom 1 relaxes towards V for global strains up to $\bar{\epsilon}_1=0.12$ (Fig. 5). This inward displacement reduces the magnitude of the major axis a_e [Eq. (8)], which can be described as a lattice "healing" process. Atom 2 initially relaxes towards V, but for strains $\bar{\epsilon}_1>0.01$, it moves away from V (Fig. 5). This motion causes atoms 3 and 4 also to relax away from V starting at $\bar{\epsilon}_1=0.04$ (Fig. 5). The rate of outward displacements of these atoms does not significantly increase until $\bar{\epsilon}_1=0.26$ [Figs. 4(c) and 5]. To assist with the visualization of the changes that occur between $\bar{\epsilon}_1=0.26$ and $\bar{\epsilon}_1=0.28$, atoms 2, 3, $3n$, 4, and $4n$ are grouped into wedge structures which are bounded by dotted lines in Fig. 4(c). The displacements in Fig. 4(c) reveal shear deformations along the edges of the wedge structures. The final atomic positions which result from these displacements correspond to the state labeled F in Figs. 2(b) and 3(b). The solid lines HP in Fig. 6 indicate the planes along which the shears occur. The (100) plane containing atom $1L$ is folded and the symmetry of the solid is lowered, which establishes a trend towards fracture.

The atomic displacements can also be analyzed in terms of the *local strains* which develop in the solid. A *local strain field* on a discrete lattice can be defined by the deformations of tetrahedra which join four nearest-neighbor atoms. The deformations are given in terms of six coordinates Q_i, $i=1,\ldots,6$. These correspond to the six normal modes of vibration of a tetrahedral molecule. Their symmetries $A_1(Q_1)$, $E(Q_2,Q_3)$, and $T(Q_4,Q_5,Q_6)$ with respect to the tetrahedral group allow them to be identified as the local strains of each tetrahedron. The coordinates

$$\begin{aligned} Q_1&=\bar{\epsilon}_{\mathrm{loc1}}+\bar{\epsilon}_{\mathrm{loc2}}+\bar{\epsilon}_{\mathrm{loc3}}, \quad \text{volume strain } \bar{\epsilon}_{\mathrm{locVOL}} \\ Q_2&=\bar{\epsilon}_{\mathrm{loc1}}-\bar{\epsilon}_{\mathrm{loc3}}, \quad \text{orthorhombic shear } \bar{\epsilon}_{\mathrm{locOS}} \end{aligned} \tag{9}$$

for a given tetrahedron are determined by taking the $\bar{x}$, $\bar{y}$, and $\bar{z}$ displacements of each of the four corner atoms and projecting them onto the following vectors:

$$Q_1:\frac{1}{2a_0}(u,-u,u;-u,u,u;u,u,-u;-u,-u,-u) \ ,$$

$$Q_2:\frac{1}{2a_0}(u,u,0;-u,-u,0;u,-u,0;-u,u,0) \ . \tag{10}$$

Since the displacements of the atoms in the $\bar{y}$ direction are negligible, $\bar{\epsilon}_{\mathrm{loc2}}=0$.

The local strains $\bar{\epsilon}_{\mathrm{locVOL}}$ and $\bar{\epsilon}_{\mathrm{locOS}}$ vary linearly with $\bar{\epsilon}_1$ for small global strains and then become larger in the region of the voids for $\bar{\epsilon}_1>0.24$. At $\bar{\epsilon}_1=0.28$, the local strains (see Fig. 7) are magnified along the planes labelled HP in Fig. 6. This is in agreement with the prediction that slip (shear deformation) in a lattice occurs along the dislocation glide planes which have normals that are closest to 45° to the axis of tensile strain.[27] Although our simulated defect is not a sharp crack, an analogy can be made with the mesoscopic theories of Kelly *et al.*[2] and Rice and Thompson[3] because the stress is focused locally around the defect in a similar way (see Sec. I). The simulated material can be viewed as ductile since the dissipation of the local strains away from the voids is by shearing rather than by cleaving.

Underlying the behavior of the defective system is the nature of the interatomic bonds. The bonds due to pairwise interactions establish certain lengths, but not necessarily specific directions, between pairs of atoms. Metallic bonds are strongly dependent on the volume which atoms occupy, rather than the separations between pairs of atoms. It is important to quantify this idea about metallic cohesion and to determine how metallic bonding defines the atomistic processes observed in the simulation.

Metallic bonding in real materials can be thought of in terms of the arrangement of the atoms. The spreading apart of the atoms tends to establish a uniform distribution in which each atom has a certain "ideal" volume and the nearest neighbors are on average all the same distance away from one another for the given atomic density in which the atoms reside. One motivation for this concept comes from linear

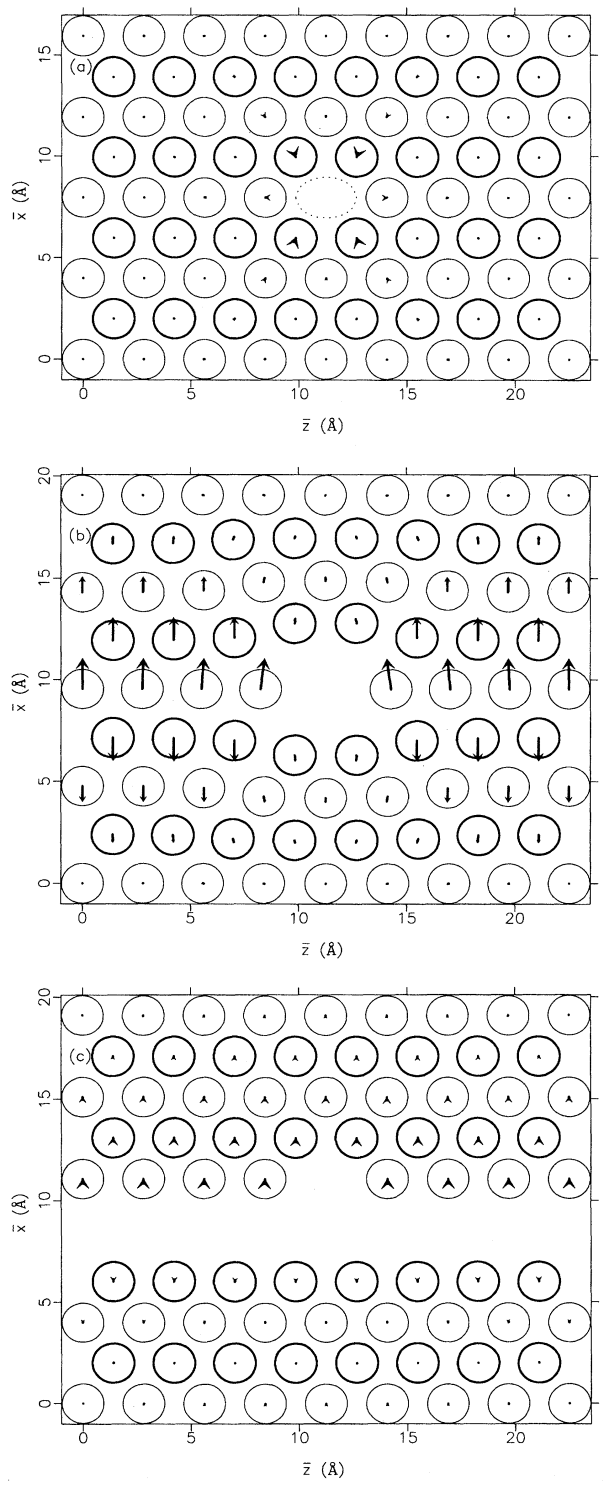

FIG. 12. Relaxed atomic positions in the pair-potential simulation at $\bar{\epsilon}_1 =$ (a) 0.000, (b) 0.196, and (c) 0.198. The vectors indicate the positions to which the atoms relax when the system is expanded by $\Delta\bar{\epsilon}_1 =$ (a) 0.000, (b) 0.002, and (c) 0.002. The atoms in planes 1 and 2 are represented by thin and thick edged circles (see Fig. 1). The ellipse delineating the defect has major and minor axes defined by Eq. (8).

elasticity theory. When a uniaxial stress is applied to an isotropic elastic material, the resulting volume change is[1]

$$\Delta V=(1-2\nu)\epsilon \ , \tag{11}$$

where ν is the Poisson ratio and ϵ is the strain in the direction of the applied stress. Metals tend to have large Poisson ratios (e.g., $\nu>\frac{1}{3}$) and therefore do not demonstrate as great an increase in V as other materials. The bonding which generates a large Poisson ratio for a metal also forces the atoms to undergo only a small volume change under uniaxial loading.

The above picture of metallic bonding can be tested by measuring the volumes of the atoms in the relaxed configurations. The local volume strains of the tetrahedra provide one estimate of the atomic volumes. The relation in Fig. 8 shows that at low global strains the volume of tetrahedron T, which links atoms 2, $2n$, 1, and the periodic image of 1 in the $\bar{y}$ direction, increases linearly with respect to strain. A more rapid increase in $\bar{\epsilon}_{\text{locVOL}}$ for T does not occur until very high global strains ($\bar{\epsilon}_1>0.24$). The volume of the remaining tetrahedra in the system behaves similarly to that of T. These observations demonstrate that the defective system exhibits a resistance to changes in uniformity of the atomic distribution. This feature of metallic bonding delays the transition to the fractured state until very high global strains and gives rise to ductile atomistic processes. The solid deforms by folding and shearing processes, rather than by separating along a fracture surface.

V. COMPARISON OF PAIR-POTENTIAL, SUTTON-CHEN GLUE, AND *AB INITIO* SIMULATIONS

The tensile test experiments on the perfect and defective systems (Sec. II) are also performed using a Morse pair potential and a Sutton-Chen glue scheme. In these simulations, the defective solid is expanded in nominal strain increments of 0.01 for low global strains, and then in increments of 0.002 for high global strains. The atoms in the defective system are relaxed until the forces on all of the atoms are smaller than 0.001 eV/Å. The strain increment and tolerance on the forces are larger in the *ab initio* calculations (Sec. IV). However, a number of tests indicated that the use of smaller increments and tolerances in the *ab initio* approach did not produce significantly different results over the major portion of the simulation.

In the simplest atomistic model of a solid, it is assumed that the atoms only interact in a pairwise fashion. The pair potential $\phi(r_{ij})$ describing these interactions depends on the distance $r=r_{ij}$ between pairs of atoms i and j. The present work employs a Morse potential:

$$\phi(r)=D(e^{-2\alpha(r-r_0)}-2e^{-\alpha(r-r_0)}) \ . \tag{12}$$

The constants α, r_0, and D are determined so that the resulting potential describes the elastic properties of the quantum mechanically simulated defective system as well as possible. The input values from the *ab initio* simulation include the equilibrium lattice constant a_0, elastic constant c_{11}, and void formation energy E_{void}. The elastic constant c_{11} is important since it is the modulus relevant to the [100] direction of deformation. The void formation energy is employed in

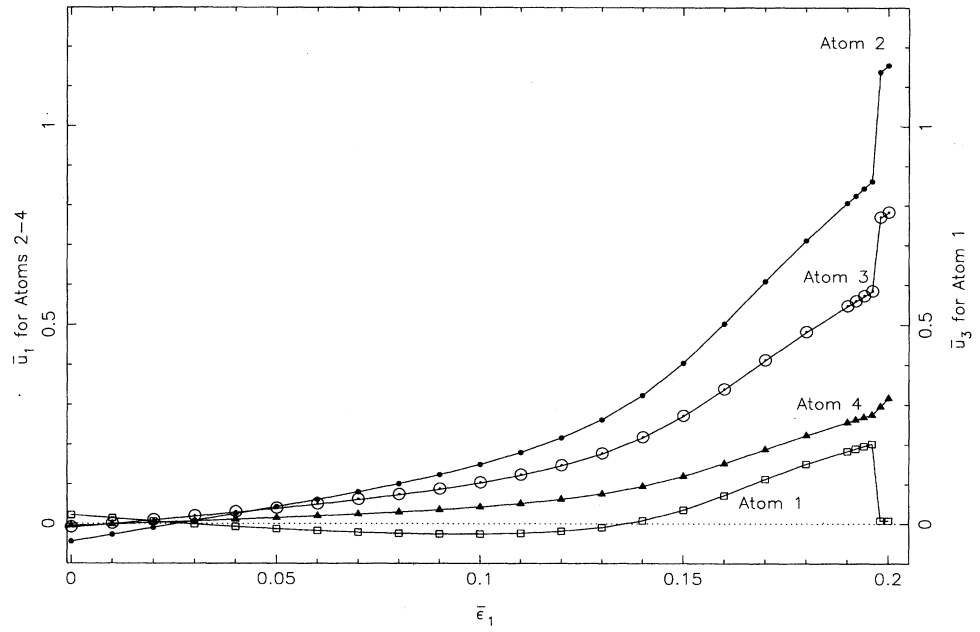

FIG. 13. Displacement $\bar{u}_3 = \bar{z}_{\text{rel}} - \bar{z}_{\text{unrel}}$ of atom 1 and $\bar{u}_1 = \bar{x}_{\text{rel}} - \bar{x}_{\text{unrel}}$ of atoms 2, 3, and 4 as a function of strain $\bar{\epsilon}_1$ in the pair-potential simulation. The variables $\bar{z}_{\text{rel}}$ ($\bar{x}_{\text{rel}}$) and $\bar{z}_{\text{unrel}}$ ($\bar{x}_{\text{unrel}}$) refer to the $\bar{z}$ ($\bar{x}$) coordinate of atom 1 (atoms 2–4) in the relaxed and unrelaxed, uniformly strained defective system, respectively. Increases in $\bar{u}_1$ and $\bar{u}_3$ indicate displacements away from the center of the voids. The displacements of atoms 1, 2, 3, and 4 are represented by squares, filled circles, open circles, and triangles, respectively.

order to reflect the defective nature of the lattice and the role of γ in Eqs. (6) and (7), for instance. The energy needed to create an atomic-scale void is defined by

$$E_{\text{void}} = E_{63} - \tfrac{63}{64} E_{64} , \tag{13}$$

where E_{63} is the total energy of the unrelaxed 63 atom (defective) supercell and E_{64} is the total energy of the 64 atom (perfect) supercell.[24] We could have relaxed the atomic positions in calculating E_{63} but the amount of relaxation would have been different for each of the potential models so that it was thought better to use identical unrelaxed positions. The calculations of E_{63} and E_{64} were performed using the *ab initio* method with the same a_0. The calculation of c_{11} was presented in Sec. III. The resulting E_{void} and c_{11} are summarized in Table III. The parameters α, r_0, and D which were derived from the *ab initio* a_0, c_{11}, and E_{void} are also included in Table III. The cutoff in all the summations was 15 Å.

Some of the problems inherent in the pair-potential approach were addressed to a certain extent by the embedded atom method[10], the Finnis-Sinclair (N-body) potentials,[9] and the effective medium theory.[11] In these "glue" schemes, each atom in the solid is embedded in a host consisting of all the other atoms. The total energy is expressed as a summation over atomic positions

$$E_{\text{tot}} = \frac{1}{2} \sum_{i \neq j} \varphi(r_{ij}) + \sum_i F_i(\rho_i) , \tag{14}$$

where F_i is the embedding energy of atom i, ρ_i is some measure of the local atomic density or effective number of nearest neighbors bonded to the atom at position $\mathbf{R}_i$, and $\varphi(r_{ij})$ is a pair potential. The embedding term can be interpreted as the energy of a given atom in a medium of appropriate density. For example, in the Finnis-Sinclair potential, F_i is proportional to the square root of ρ_i.

In the Sutton-Chen glue scheme,[28] the total energy per supercell is given by

$$E_{\text{tot}} = \frac{1}{2} \sum_{i \neq j} \varepsilon \left(\frac{a}{r_{ij}} \right)^n - c\varepsilon \sum_i \rho_i^{1/2} , \tag{15}$$

$$\rho_i = \sum_{j \neq i} \left(\frac{a}{r_{ij}} \right)^m , \tag{16}$$

where c is a positive dimensionless parameter, ε is a parameter with the dimensions of energy, a is a parameter with the dimensions of length, ρ_i is the local atomic density around atom i, and m and n are positive integers. The first summation in Eq. (15) is the contribution due to a pair potential describing the repulsion of the atoms at short distances. The second summation is the embedding (N-body) term which is a square-root function of the atomic density. It represents the multiatom nature of metallic bonding.[29]

Apart from the exponents m and n, the Sutton-Chen potential Eq. (15) has two adjustable parameters c and ε. Note that a is an arbitrary length and any change of a can be canceled by appropriate changes in c and ε. Thus once m and n are chosen, there is no way of fitting the three quantities a_0, c_{11}, and E_{void} exactly as we did for the Morse potential: one has to do a best fit. The results for $(m,n) = (5,9)$, as recommended for aluminum by Sutton and Chen,[29] are summarized in Table IV. The exponents $(m,n) = (6,7)$ were also tried but did not give as good an overall fit to the elastic properties of the *ab initio* simulated aluminum. The cutoff of the potential was 20 Å.

As in the quantum mechanical simulations, the stress-strain relations start at about zero, increase, and then reach a maximum (Figs. 9 and 11). In the pairwise model, the maximum tensile stress sustained by the defective solid is $\sigma_{\max}(D) = 8.75 \pm 0.01$ GPa, which is about 14% lower than $\sigma_{\max}(P) = 10.17 \pm 0.01$ GPa sustained by the perfect solid (Fig. 9). In the glue simulation, the maximum tensile stress

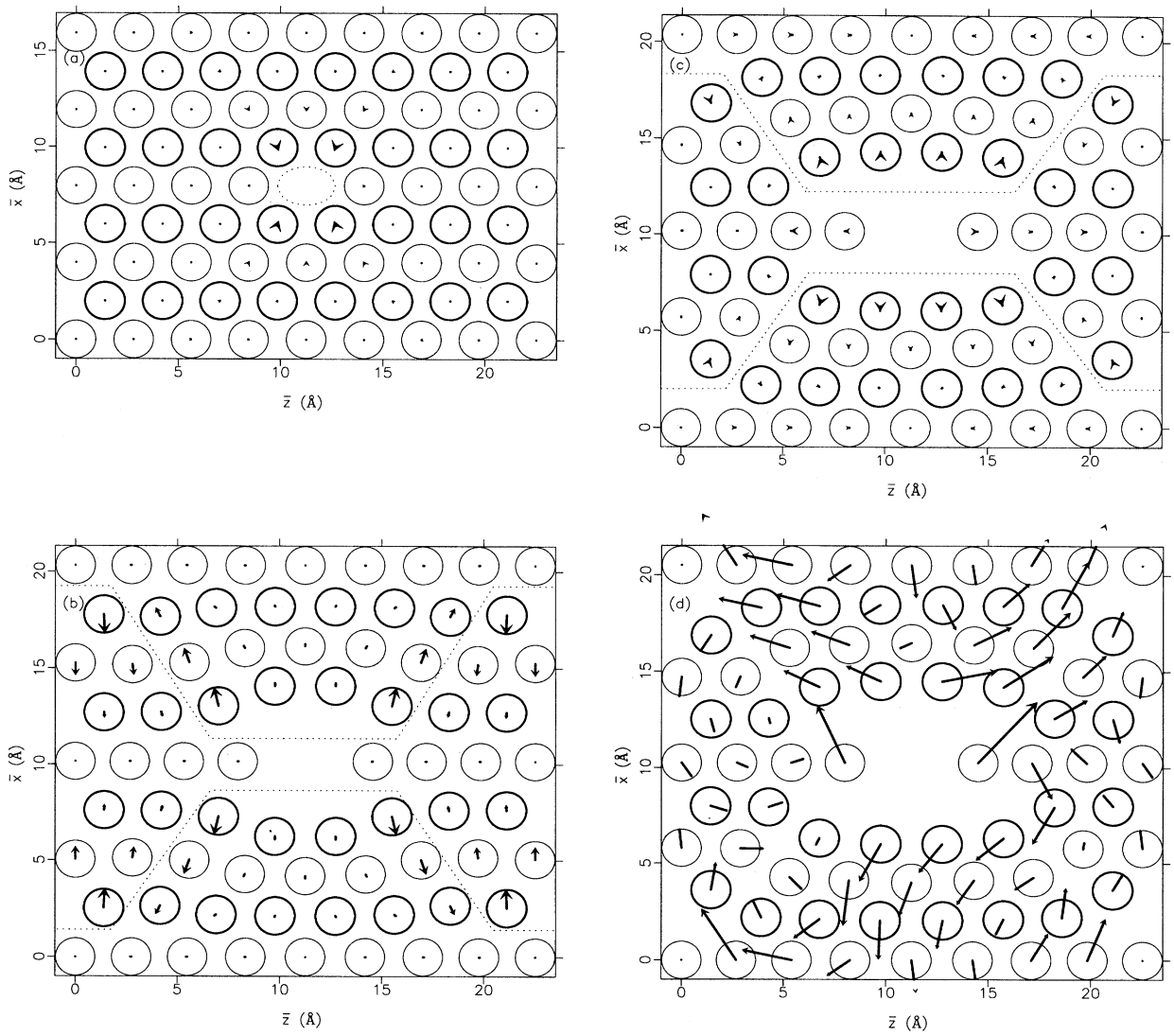

FIG. 14. Relaxed atomic positions in the glue simulation at $\bar{\epsilon}_1 =$ (a) 0.000, (b) 0.274, (c) 0.276, and (d) 0.286. The vectors indicate the positions to which the atoms relax when the system is expanded by $\Delta\bar{\epsilon}_1 =$ (a) 0.000, (b) 0.002, (c) 0.002, and (d) 0.002. The atoms in planes 1 and 2 are represented by thin and thick edged circles. The ellipse delineating the defect has major and minor axes defined by Eq. (8). In (c) and (d), shear deformations occur along the sides of the wedge structures which are bounded by the dotted lines and contain atoms 2, $2n$, 3, $3n$, $3nn$, 4, $4n$, and $4nn$.

sustained by the defective solid is $\sigma_{\max}(D)=8.29\pm0.05$ GPa, which is about 9% lower than $\sigma_{\max}(P)=9.15\pm0.05$ GPa sustained by the perfect solid (Fig. 11). These reductions in $\sigma_{\max}$ are larger than in the *ab initio* simulation and indicate that the defects have a greater effect on the strength of the empirically simulated metal.

The defective solid in the pairwise model suffers an abrupt brittle fracture at $\bar{\epsilon}_1=0.198$ with the stress dropping effectively to zero (Fig. 9). However, in general failure can occur in a number of discrete steps, as observed in the glue simulation (see below) and presumably in the *ab initio* simulation, though the latter was not carried to that stage. Thus one can ask whether the failure is abrupt from one configuration to another, analogous to a first-order phase transition with hysteresis, or whether it is a continuous gliding transition where some generalized coordinate goes through an instability analogous to a second-order phase transition. To demonstrate the hysteresis explicitly, we have run the simulation backwards from the relaxed configuration for the pair potential (PP) from $F_{\rm PP}$ ($\bar{\epsilon}_1=0.198$) to smaller values of $\bar{\epsilon}_1$ as shown in Fig. 9. The compression curve returns to the extension curve for $\bar{\sigma}_1(\bar{\epsilon}_1)$ at $\bar{\epsilon}_1=0.130$ (Fig. 9).

At very high global strains, the defective system in the glue simulation undergoes first-order structural transitions at $\bar{\epsilon}_1=0.276$ and $\bar{\epsilon}_1=0.288$. In both cases, the total energy (Fig. 10) and the stress (Fig. 11) decrease discontinuously. The energies of the configurations generated by the compression of the failed state at $F_{\rm glue}$ (dashed line in Fig. 10), are initially lower than the energies of the states determined under tensile strain. These lower energy configurations

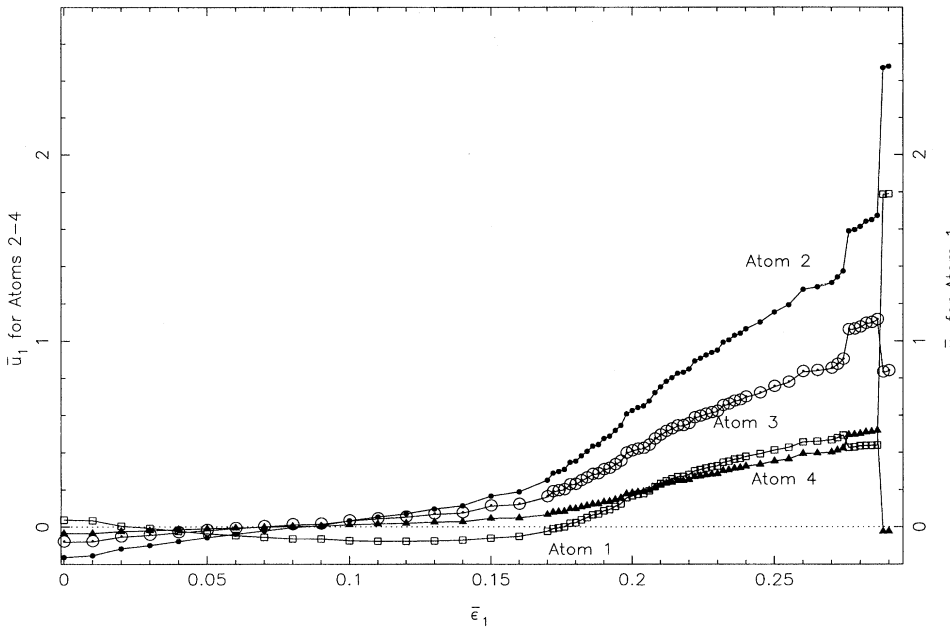

FIG. 15. Displacement $\bar{u}_3 = \bar{z}_{\text{rel}} - \bar{z}_{\text{unrel}}$ of atom 1 and $\bar{u}_1 = \bar{x}_{\text{rel}} - \bar{x}_{\text{unrel}}$ of atoms 2, 3, and 4 as a function of strain $\bar{\epsilon}_1$ in the glue simulation. The variables $\bar{z}_{\text{rel}}$ ($\bar{x}_{\text{rel}}$) and $\bar{z}_{\text{unrel}}$ ($\bar{x}_{\text{unrel}}$) refer to the $\bar{z}$ coordinate of atom 1 (atoms 2–4) in the relaxed and unrelaxed, uniformly strained defective system, respectively. Increases in $\bar{u}_1$ and $\bar{u}_3$ indicate displacements away from the center of the voids. The displacements of atoms 1, 2, 3, and 4 are represented by squares, filled circles, open circles, and triangles, respectively.

confirm that the states determined under tensile strain are metastable for $\bar{\epsilon}_1 > \epsilon_{\max}(D)$ and that the transitions at $\bar{\epsilon}_1 = 0.276$ and $\bar{\epsilon}_1 = 0.288$ are first order in nature. In addition, the compression curve beginning with the relaxed state at $\bar{\epsilon}_1 = 0.276$ (dotted line in Fig. 10), intersects the original tensile energy-strain curve at $\bar{\epsilon}_1 = 0.140$. Hence, the states under increasing tensile strain for $\bar{\epsilon}_1 > 0.140$ are metastable.

The relaxed configurations at several levels of tensile strain are visualized in Fig. 12 (pairwise model) and Fig. 14 (glue model). The motions of atoms 1, 2, 3, and 4 are given in Fig. 13 (pairwise model) and Fig. 15 (glue model), following the atom numbering of Fig. 1. At zero global strain in the pair-potential and glue simulations [Figs. 12(a) and 14(a)], atom 1 relaxes slightly away from and atom 2 relaxes slightly towards the center of the voids (referred to as V). This is contrary to the behavior in the *ab initio* calculations where atoms 1 and 2 both relax toward V [Fig. 4(a)]. Atoms 3 and 4 in the empirically based models also relax towards V, but their motions are small. As the global strain increases, atom 1 moves towards V and atoms 2, 3, $3n$, 4, and $4n$ move away from V. The motion of atom 1 in the empirically based models causes the major axis of the ellipse representing the voids [Eq. (8)] to decrease, which can be viewed as a lattice healing process. However, this trend reverses since atom 1 relaxes away from V beginning at $\bar{\epsilon}_1 = 0.100$ in the pairwise model (Fig. 13) and at $\bar{\epsilon}_1 = 0.130$ in the glue model (Fig. 15). A similar lattice healing process occurs in the *ab initio* simulation and it reverses at $\bar{\epsilon}_1 = 0.12$ (Fig. 5).

The rate of outward displacement of atoms 1–4 increases significantly for $\bar{\epsilon}_1 > 0.140$ in the pair-potential approach (Fig. 13) and $\bar{\epsilon}_1 > 0.170$ in the glue approach (Fig. 15). These outward movements mark a strong void expansion prior to the failure at $\bar{\epsilon}_1 = 0.198$ in the pair-potential model and $\bar{\epsilon}_1 = 0.288$ in the glue model. The void expansion in the *ab initio* simulation occurs at a higher global strain since the outward motions of atoms 1–4 do not increase dramatically until $\bar{\epsilon}_1 > 0.24$ (Fig. 5), which is much closer to the failure strain.

Before the failure of the defective solid in the pairwise model, atoms 2, 3, $3n$, 4, and 4n generally move away from the voids. The remaining atoms in the system show little displacement from their uniformly strained fcc sites. However, at the point of fracture, atoms 2, 3, $3n$, 4, and $4n$ relax very little [Fig. 12(b)]. The other atoms in the supercell undergo large changes in position. These motions form a (100) fracture surface [Fig. 12(c)], which breaks the symmetry of the solid in the plane $\bar{x} = \frac{1}{2}|\mathbf{a}_1|$. In contrast to this brittle failure, the defective solid in the quantum mechanical simulation will eventually fail by ductile processes, namely, shearing and folding of planes of atoms (Fig. 6).

Prior to the first structural transition at $\bar{\epsilon}_1 = 0.276$ in the glue simulation, atoms 2, 3, $3n$, 4, and $4n$ generally move away from the voids. The remaining atoms in the system show little displacement from their uniformly strained fcc sites. To help identify the changes in the atomic configuration at $\bar{\epsilon}_1 = 0.276$, a dotted line is drawn around groups of atoms in Figs. 14(b) and 14(c). These wedge structures include atoms 2, $2n$, 3, $3n$, $3nn$, 4, $4n$, and $4nn$. At the transition, atoms 2, 3, $3n$, 4, and $4n$ relax very little, but atoms $2n$, $3nn$, and $4nn$ move to the same position in the $\bar{x}$ direction as atoms 2, $3n$, and $4n$, respectively [Fig. 14(b)]. This smooths the surfaces of the wedges, especially the section containing atoms 2 and $2n$, but it leaves atom 1 with few nearest neighbors [Fig. 14(c)]. These processes can be characterized as shear deformations along the sides of the wedges. The planes on which these shears develop are also identified as the lines QP in Fig. 16(a). Neither wedge structures nor shear planes are formed in the pair-potential simulation.

The coordination number of atom 1 in the glue simulation decreases following the shear deformation at $\bar{\epsilon}_1 = 0.276$. However, the relaxations at $\bar{\epsilon}_1 = 0.288$ break the symmetry of

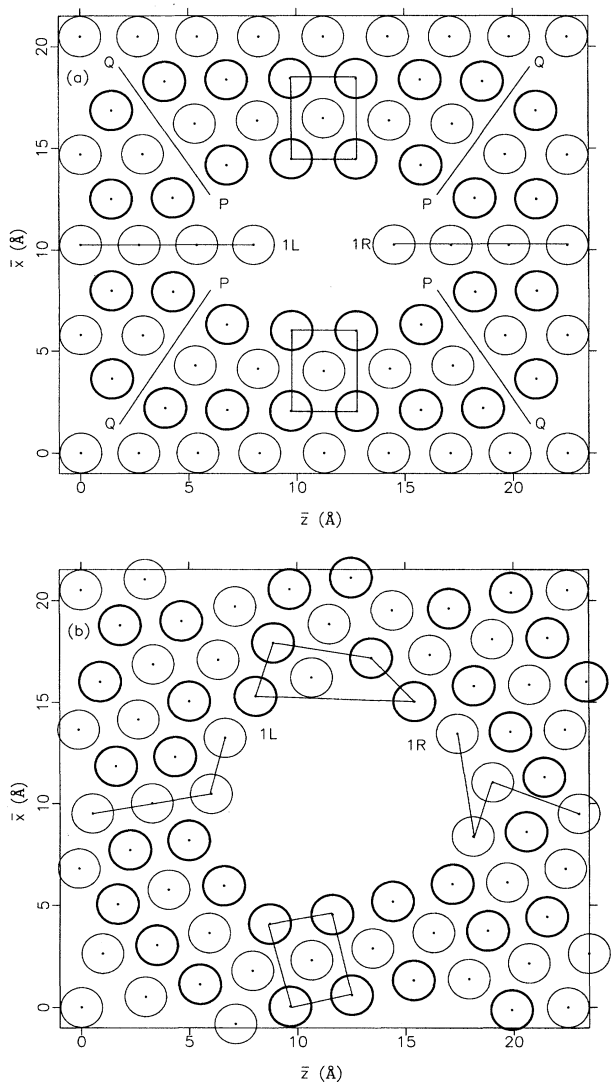

FIG. 16. (a) Relaxed atomic positions at $\bar{\epsilon}_1=0.286$ in the glue simulation. Shear deformations at $\bar{\epsilon}_1=0.276$ occur along the planes denoted by the lines QP. (b) Relaxed atomic configuration at F_{glue} ($\bar{\epsilon}_1=0.288$) in the glue simulation. In both figures, the lines connecting groups of atoms indicate how the atomic structure changes following failure.

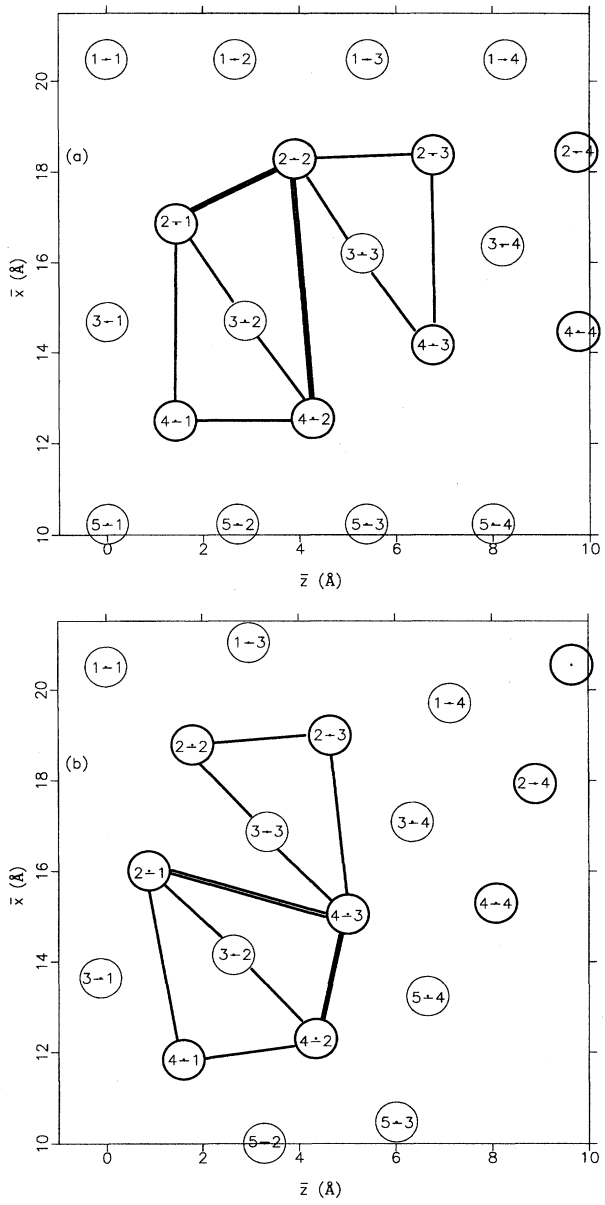

FIG. 17. (a) Relaxed atomic positions at $\bar{\epsilon}_1=0.286$ in the glue simulation. (b) Relaxed atomic configuration at F_{glue} ($\bar{\epsilon}_1=0.288$) in the glue simulation. In both figures, the lines connecting groups of atoms indicate how the atomic structure changes following failure. The atoms are labeled by *i-j* for the *j*th atom in row *i* of the original unstrained system.

the system in the planes $\bar{z}=\frac{1}{2}|\mathbf{a}_3|$ and $\bar{x}=\frac{1}{2}|\mathbf{a}_1|$ and send atoms $1L$ and $1R$ (i.e., atom 1 in the left and right halves of the supercell) to sites of higher coordination number [Fig. 14(d)]. The final relaxed positions at $\bar{\epsilon}_1=0.286$ and $\bar{\epsilon}_1=0.288$ are compared in Fig. 16. The solid lines connecting groups of atoms help identify the changes in structure. The box of atoms in the lower half of the supercell is rotated from its original orientation and the box of atoms in the upper half of the supercell is deformed. The (100) plane of atoms containing atoms $1L$ and $1R$ is severely folded. The original void is larger and secondary voids are nucleated at the edges of the supercell. These processes resemble those at $\bar{\epsilon}_1=0.28$ [Fig. 4(c)] in the *ab initio* simulation, since there are shear events along the edges of wedge structures. However, atoms $2nn$, $3nn$, and $4nn$ are not contained within the wedges in the *ab initio* method, whereas atoms $2nn$, $3nn$, and $4nn$ are included inside the wedges in the glue simulation. Atoms $1L$ and $1R$ are not as isolated in Fig. 6 as they are in Fig. 14(c). The (100) plane containing atom $1L$ in Fig. 6 is slightly folded. The folding of this plane does not occur in the glue simulation until the critical failure strain is attained [Fig. 16(b)].

The atomic displacements can also be analyzed in terms of the local strains which were defined in Sec. IV. We are

interested in the local volume strains for our discussion of metallic bonding in Sec. VI and in the local shear strains for our discussion of the mechanical behavior.

Although the local strains near the voids become magnified as the failure strain is approached, the response of the defective system in the pairwise model differs from that in the *ab initio* calculations. The failure of the system in the pairwise case is accompanied by a reduction of the local strains within each of the separated sections to small values. Extended local shear deformations, as observed in the quantum mechanical simulation (Fig. 7), do not develop in the pair-potential calculations. The absence of shear failure indicates brittle behavior in the pairwise approach by analogy with the mesoscopic theories discussed in Sec. I.

The first structural transition in the glue method at $\bar{\epsilon}_1=0.276$ magnifies the local shear strains along the planes QP shown in Fig. 16(a). These extended shear deformations are in agreement with the prediction that slip in a lattice occurs along the dislocation glide planes with normals which are closest to 45° to the tensile axis.[27] Since the local strains in the vicinity of the voids are dissipated by shearing rather than by cleavage, the simulated material can be classified as ductile by analogy with the mesoscopic theories discussed in Sec. I. Similar shear processes were observed in the *ab initio* simulation.

VI. CONCLUSIONS ABOUT POTENTIAL MODELS AND FEATURES OF METALLIC BONDING

Underlying the behavior of the defective system in the *ab initio*, pairwise, and glue simulations is the nature of the interatomic bonds. As discussed in Sec. IV, a distinguishing feature of metallic cohesion is the tendency of the atoms in a metal to distribute themselves as uniformly as possible. A measure of this uniformity are the local volume strains of tetrahedra linking four nearest neighbors. In the pair-potential simulation, the local volume strains increase at first linearly with $\bar{\epsilon}_1$ and then more rapidly from about $\bar{\epsilon}_1=0.100$. In the glue simulation, they increase at first linearly with $\bar{\epsilon}_1$ and then more rapidly from about $\bar{\epsilon}_1=0.170$. This greater rate of increase corresponds to an unphysical void expansion at strains well before failure. For example, the variation of the local volume strain of tetrahedron T linking atoms 2, $2n$, 1, and the periodic image of 1 in the $\bar{y}$ direction is shown in Fig. 8. Note that $\bar{\epsilon}_{\mathrm{locVOL}}$ for T in the *ab initio* simulation does not show a similar increase until a higher global strain ($\bar{\epsilon}_1=0.26$) much nearer failure.

The observations described above demonstrate that the defective system in the *ab initio* simulation exhibits the greatest resistance to changes in the uniformity of the atomic distribution. This feature of metallic bonding delays the transition to the fractured state until very high global strains and gives rise to ductile atomistic processes. The pairwise simulation gives a poorer representation of metallic bonding since the atomic distributions deviate from uniformity at a much lower strain than in the quantum mechanical simulation. The solid in the pairwise model cleaves into two sections which discontinuously reduces the uniformity of the whole system. In contrast, the solid in the quantum mechanical simulation responds to the applied strain by trying to maintain an even distribution of atoms in all parts of the system. Hence, it deforms by folding and shearing processes, rather than by separating along a fracture surface. The behavior in the glue and *ab initio* models is qualitatively similar, but the configurations in the former case deviate from uniformity at a much lower global strain of 0.17, compared to 0.26.

Structural changes are not so well described by the Sutton-Chen potential, though this model is a step in the right direction from the purely pairwise approach. In a nearly-free-electron metal such as aluminum, the local electron density, or alternatively the local atomic density ρ_i or its inverse, the local atomic volume ρ_i^{-1}, is an important determinant of the energy. This fact is reinforced by the very smooth variation of $\bar{\epsilon}_{\mathrm{locVOL}}$ in the *ab initio* calculations. The Sutton-Chen glue model might reproduce the *ab initio* results better if it was modified to improve the calculation of the local atomic volume. Other glue schemes can also be tested using the quantum mechanical results as a database.[30]

VII. CONCLUSIONS ABOUT LOCAL DEFORMATIONS

The first significant characteristic of the local deformations is the rapid movement of the central atoms away from the voids. As discussed in earlier sections, these displacements correspond to the expansion of the voids. In the *ab initio* simulation, the expansion does not occur until just before failure. In contrast, this behavior begins at strains of about 60% of the failure strain in the pair and glue simulations.

A second feature of the local atomic rearrangements are the slip processes which occur following the failure of the system in the glue simulation. The upper left corner of the supercell is reproduced in Fig. 17. We specify the atoms by i-j for the jth atom in row i of the original unstrained system. The cell consisting of atoms 2-1, 4-1, 4-2, and 2-2 [Fig. 17(a)] reconfigures itself to include atoms 2-1, 4-1, 4-2, and 4-3 after failure [Fig. 17(b)]. Atom 4-3 takes the topological place of atom 2-2, which is equivalent to slip along the line labeled QP in Fig. 16(a). We see the gradual nucleation of a dislocation in contrast with the sudden click events associated with grain boundary sliding in germanium.[31]

The above observations of the motions in the glue simulation improve our understanding of the *ab initio* calculations. The geometry across the line HP in Fig. 6 is exactly the same as across QP in Fig. 16(a). The same type of slip would have occurred in the *ab initio* simulation if we had been able to carry the computations further. To check this, we took the coordinates from the final positions following failure in the glue simulation and relaxed them to a ground state configuration using the *ab initio* approach. The resulting structure was nearly the same as in Fig. 16(b).

ACKNOWLEDGMENTS

This research was supported by the Natural Sciences and Engineering Research Council (Canada) and the Sciences and Engineering Research Council (U.K.). This paper resulted from a collaboration within, and was partially funded by, the Human Capital and Mobility Network on "*Ab initio* (from electronic structure) calculation of complex processes in materials" (Contract No. ERBCHRXCT930369).

*Present address: Department of Physics, Massachusetts Institute of Technology, Cambridge, Massachusetts, 02139.
†Present address: Molecular Simulations Limited, 240/250 The Quorum, Barnwell Road, Cambridge, CB5 8RE, United Kingdom.
‡Present address: School of Mathematics and Physics, The Queen's University of Belfast, Belfast, BT7 1NN, Northern Ireland.

[1] A. Kelly and N.H. Macmillan, *Strong Solids* (Oxford, London, 1986).
[2] A. Kelly, W. Tyson, and A.H. Cottrell, Philos. Mag. **15**, 567 (1967).
[3] J.R. Rice and R. Thomson, Philos. Mag. **29**, 78 (1974).
[4] I.H. Lin, J. Mater. Sci. Lett. **2**, 295 (1983).
[5] R.W.K. Honeycombe, *The Plastic Deformation of Metals* (Edward Arnold, London, 1984).
[6] M.C. Payne, M.P. Teter, D.C. Allan, T.A. Arias, and J.D. Joannopoulos, Rev. Mod. Phys. **64**, 1045 (1992).
[7] V. Heine, in *Solid State Physics*, edited by H. Ehrenreich, F. Seitz, and D. Turnbull (Academic, New York, 1980), Vol. 35.
[8] M.J. Puska, in *Many-atom Interactions in Solids*, edited by R.M. Nieminen, M.J. Puska, and M.J. Manninen (Springer-Verlag, Berlin, 1990).
[9] M.W. Finnis and J.E. Sinclair, Philos. Mag. A **50**, 45 (1984).
[10] M.S. Daw and M.I. Baskes, Phys. Rev. Lett. **50**, 1285 (1983).
[11] K.W. Jacobsen, J.K. Nørskov, and M.J. Puska, Phys. Rev. B **35**, 7423 (1987).
[12] L. Kleinman and D.M. Bylander, Phys. Rev. Lett. **48**, 1425 (1980); J.S. Lin, A. Qteish, M.C. Payne, and V. Heine, Phys. Rev. B **47**, 4174 (1993).
[13] J. Perdew and A. Zunger, Phys. Rev. B **23**, 5048 (1981).
[14] C.-L. Fu and K.-M. Ho, Phys. Rev. B **28**, 5480 (1983).
[15] R.J. Needs, R.M. Martin, and O.H. Nielsen, Phys. Rev. B **33**, 3778 (1986).
[16] M.P. Teter, M.C. Payne, and D.C. Allan, Phys. Rev. B **40**, 12 225 (1989).
[17] H. Hellmann, *Einfuhrung in die Quantumchemie* (Deutick, Leipzig, 1937); R.P. Feynman, Phys. Rev. **56**, 340 (1939).
[18] P.P. Ewald, Ann. Phys. (Leipzig) **54**, 519, 557 (1917); **64**, 253 (1921).
[19] O.H. Nielsen and R.M. Martin, Phys. Rev. B **32**, 3792 (1985).
[20] H.J. Monkhorst and J.D. Pack, Phys. Rev. B **13**, 5188 (1976).
[21] G.P. Francis and M.C. Payne, J. Phys. Condens. Matter **2**, 4395 (1990).
[22] P.K. Lam and M.L. Cohen, Phys. Rev. B **24**, 4224 (1981).
[23] G.N. Kamm and G.A. Alers, J. Appl. Phys. **35**, 327 (1964).
[24] M.J. Gillan, J. Phys. Condens. Matter **1**, 689 (1989); A. De Vita and M.J. Gillan, *ibid.* **3**, 6225 (1991).
[25] W.R. Tyson and W.A. Miller, Surf. Sci. **62**, 267 (1977).
[26] N. Gane, Proc. R. Soc (London) A **317**, 367 (1970).
[27] M.F. Ashby and D.R.H. Jones, *Engineering Materials: An Introduction to Their Properties & Applications* (Pergamon, Oxford, 1980).
[28] A.P. Sutton and J. Chen, Philos. Mag. Lett. **61**, 139 (1990).
[29] V. Heine, I.J. Robertson, and M.C. Payne, Philos. Trans. R. Soc. (London) A **334**, 393-405 (1991).
[30] The relaxed atomic positions, stresses, and total energies of the present *ab initio*, pair, and glue simulations are available for comparison. Ftp to tcm1.phy.cam.ac.uk, log on as anonymous, and download the files in the directory /ftp/pub/vbd10.
[31] G.P. Francis, C. Molteni, M.C. Payne, and V. Heine (unpublished).